Unmixing dynamic PET images with a PALM algorithm

Yanna Cruz Cavalcanti[(1)], Thomas Oberlin[(1)], Nicolas Dobigeon[(1)] and Clovis Tauber[(2)]

[(1)] University of Toulouse, IRIT/INP-ENSEEIHT, Toulouse, France
[(2)] UMRS INSERM U930 - Université de Tours, 37032 Tours, France
firstname.lastname@enseeiht.fr, clovis.tauber@univ-tours.fr

***Abstract*—Unmixing is a ubiquitous task in hyperspectral image analysis which consists in jointly extracting typical spectral signatures and estimating their respective proportions in the voxels, providing an explicit spatial mapping of these elementary signatures over the observed scene. Inspired by this approach, this paper aims at proposing a new framework for analyzing dynamic positron emission tomography (PET) images. More precisely, a PET-dedicated mixing model and an associated unmixing algorithm are derived to jointly estimate time-activity curves (TAC) characterizing each type of tissues, and the proportions of those tissues in the voxels of the imaged brain. In particular, the TAC corresponding to the specific binding class is expected to be voxel-wise dependent. The proposed approach allows this intrinsic spatial variability to be properly modeled, mitigated and quantified. Finally, the main contributions of the paper are twofold: first, we demonstrate that the unmixing concept is an appropriate analysis tool for dynamic PET images; and second, we propose a novel unmixing algorithm allowing for variability, which significantly improves the analysis and interpretation of dynamic PET images when compared with state-of-the-art unmixing algorithms.**

I. Introduction

Dynamic positron emission tomography (PET) is a medical imaging technique that provides time-activity curves (TACs) representing the variations over time of the concentration of a radiotracer in the body. It yields useful quantitative information on the physiological and biochemical processes. Nevertheless, dynamic PET images of the brain suffer from a relatively low spatial resolution along with a high statistical noise due to their short intervals of acquisition, making image analysis a challenging task. To overcome these limitations, several factorial methods have been proposed to analyze dynamic PET images of the brain, including principal component analysis (PCA) and independent component analysis (ICA) [1]. These techniques aims at linearly decomposing the measured voxel TACs into a set of elementary signatures and associated weights quantifying the respective relevance of these signatures within each voxel. Interestingly, these weights could provide a surrogate sub-voxel mapping of the elementary signatures, as a way to face with partial volume effects. However, PCA and ICA assumes statistical uncorrelation or independence of the elementary signatures, which could be rarely ensured in practice. Moreover within a specific binding region (SBR), the exchange rate of tracer between the specific binding compartment and the free compartment may fluctuate [2]–[4], inducing spatial variations on the considered elementary signature.

Part of this work has been supported by CAPES.

Meanwhile, linear unmixing has been advocated as a relevant and efficient technique to analyze multi-band images acquired in various applicative contexts, ranging from Earth science [5] to experimental physics [6]. Contrary to PCA and ICA, this concurrent factorial technique is specifically suited for non-negative data and does not require any statistical assumptions. Akin to non-negative matrix factorization techniques [7], it only imposes the non-negativity of the elementary signatures (herein referred to as *endmembers*) and mixing coefficients (or *abundances*), providing a constructive part-based decomposition of the multivariate data. In addition, driven by the ease of interpretability, linear unmixing generally looks for an exhaustive description of the data by imposing an additional sum-to-one constraint to abundance coefficients associated with each measurement.

Up to authors' knowledge, this work consists of the first attempt to demonstrate the relevance of linear unmixing to analyze dynamic PET images. Besides, inspired by recent works conducted in the hyperspectral image literature to describe spatial variability of the endmembers [8], the proposed model allows the SBR endmember to be voxel-wise dependent, explaining the variations of the exchange rate of the tracer. More precisely, taking advantage of available typical signatures associated with the SBR, this intrinsic variability is physically described by decomposing it on a pre-determined subspace identified by a principal component analysis. Finally, in addition to the endmember signatures and corresponding abundances, the resulting unmixing algorithm is able to recover the SBR endmember variability assumed to be spatially sparse.

The paper is organized as follows. The observation model is described in Section II. Section III presents the PALM-based algorithm designed to estimate the endmembers, the abundances and the variability maps. Simulation results obtained with synthetic yet realistic dynamic PET images are reported in Section IV. Section V concludes the paper.

ISBN 978-0-9928626-7-1

II. Problem Statement

A. Observation model

Let $\mathbf{x}_n$ denote the TAC associated with the n_{th} voxel in a 3d PET image acquired in L time-frames when the partial volume effect is neglected, i.e., without considering the spatial blurring induced by the point spread function (PSF) of the instrument. Each TAC is assumed to be a linear combination of K endmembers $\mathbf{m}_k$

$$\mathbf{x}_n = \sum_{k=1}^{K} \mathbf{m}_k a_{k,n} \tag{1}$$

where $\mathbf{m}_k = [m_{1,k}, \ldots, m_{L,k}]^T$ denotes the TAC from a pure voxel of the kth tissue type, $a_{k,n}$ is the proportion of the kth signature in the nth voxel. The endmember signatures $\mathbf{m}_k$ ($k = 1, \ldots, K$) can for instance correspond to the kinetic of the radiotracer in gray matter without specific binding, white matter, blood and gray matter with specific binding. In the case considered in this study, the variation of the specific binding endmember (SBE) denoted $\mathbf{m}_1$ will be modeled as a spatially-variant additive perturbation affecting a nominal SBE signature $\bar{\mathbf{m}}_1$ according to the linear expansion

$$\mathbf{m}_1 = \bar{\mathbf{m}}_1 + \sum_{i=1}^{N_v} b_{i,n}\mathbf{v}_i \tag{2}$$

The $L \times N_v$ matrix $\mathbf{V} = [\mathbf{v}_1, \ldots, \mathbf{v}_{N_v}]$ gathers N_v basis elements used to describe the SBE variability. Similarly to the approach proposed in [9], the nominal SBE signature $\bar{\mathbf{m}}_1$ and the basis elements $\mathbf{v}_i$ ($i = 1, \ldots, N_v$) can be identified in a pre-processing step by conducting a PCA on a learning set composed of measured or simulated SBE TACs. Finally, the coefficients $b_{i,n}$ quantifies the variability associated with the ith elements in the nth voxel, explicitly leading to a spatially variation of the SBE. Coupling (1) with the spatially varying SBE in (2), results in the following so-called perturbed SBE linear mixing model (PSBE-LMM)

$$\mathbf{x}_n = a_{1,n}\left(\bar{\mathbf{m}}_1 + \sum_{i=1}^{N_v} b_{i,n}\mathbf{v}_i\right) + \sum_{k=2}^{K} a_{k,n}\mathbf{m}_k. \tag{3}$$

Furthermore, this work proposes to handle the partial volume effect that affects PET images by combining this PSBE-LMM with a spatially invariant PSF. The resulting blurring matrix $\mathbf{H} \in \mathbb{R}^{N\times N}$ is then assumed to be a block-circulant matrix with circulant blocks. Using standard matrix notations, the set of measurements can finally be written as

$$\mathbf{Y} = \mathbf{MAH} + \underbrace{\Big[\mathbf{E}_1\mathbf{A} \circ \mathbf{VB})\Big]\mathbf{H}}_{\Delta} + \mathbf{R}, \tag{4}$$

where $\mathbf{Y} = [\mathbf{y}_1, \ldots, \mathbf{y}_N]$ is an $L \times N$ matrix containing the N measured TACs, $\mathbf{M} = [\bar{\mathbf{m}}_1, \ldots, \mathbf{m}_K]$ is an $L \times K$ matrix containing the endmember signatures, $\mathbf{A}$ is a $K \times N$ matrix composed of the abundance vectors $\mathbf{a}_n$, "$\circ$" is the Hadamard point-wise product, $\mathbf{E}_1$ is the matrix $[\mathbf{1_{L,1}0_{L,K-1}}]$, $\mathbf{B}$ is the $N_v \times N$ matrix containing the internal abundances $\mathbf{b}_n = [b_{1,n}, \ldots, b_{N_v,n}]$ and $\mathbf{R}$ is a $L \times N$ matrix which stands for a residual term accounting for acquisition noise and modeling errors, herein considered additive, Gaussian with zero mean the noise. Moreover, the direct model (4) is complemented with the following constraints

$$\begin{gathered}\mathbf{A} \succeq \mathbf{0}_{K,N},\ \mathbf{A^T}\mathbf{1}_k = \mathbf{1}_N, \\ \mathbf{M} \succeq \mathbf{0}_{L,K} \text{ and } \mathbf{B} \succeq \mathbf{0}_{N_v,N}\end{gathered} \tag{5}$$

where $\succeq$ defines the component-wise inequality. In other words, the abundance coefficients $a_{k,n} \in [0, 1]$ are assumed to be positive and summing to 1 for each voxel, providing a close description of the voxel TAC. The variability is also assumed to be positive since a systematic negative bias will be introduced on the nominal SBE $\bar{\mathbf{m}}_1$. This constraint allows one to overcome the high correlation between the remaining TAC endmembers and $\sum_{i=1}^{N_v} \mathbf{v}_i b_{i,n}$ when $b_{i,n}$ is negative.

B. Problem formulation

The PSBE-LMM (4) is combined with the constraints (5) to derive a constrained optimization problem. The estimation of $\mathbf{M}$, $\mathbf{A}$, $\mathbf{B}$ requires a proper cost function. Since the residual matrix $\mathbf{R}$ is assumed to be composed of independent and identically Gaussian distributed entries, the data-fitting term can be derived by considering the Frobenius distance $\|\cdot\|_F^2$ between the observations $\mathbf{Y}$ and the reconstructed data $\mathbf{MAH} + \Delta$. Besides, since the problem is ill-posed and non-convex, additional regularizers are mandatory. *A priori* knowledge on $\mathbf{M}$, $\mathbf{A}$ and $\mathbf{B}$ is taken into account through the penalization functions $\Psi(\cdot)$, $\Phi(\cdot)$ and $\Omega(\cdot)$, respectively. The optimization problem is then defined as

$$(\hat{\mathbf{M}}, \hat{\mathbf{A}}, \hat{\mathbf{B}}) \in \underset{\mathbf{M},\mathbf{A},\mathbf{B}}{\arg\min}\, \mathcal{J}(\mathbf{M}, \mathbf{A}, \mathbf{B}) \text{ s.t. } (5) \tag{6}$$

with

$$\begin{aligned}\mathcal{J}(\mathbf{M}, \mathbf{A}, \mathbf{B}) = \frac{1}{2}\left\|\mathbf{Y} - \mathbf{MAH} - \Big[\mathbf{E}_1\mathbf{A} \circ \mathbf{VB})\Big]\mathbf{H}\right\|_F^2 \\ +\alpha\Phi(\mathbf{A}) + \beta\Psi(\mathbf{M}) + \lambda\Omega(\mathbf{B})\end{aligned}$$

where the penalization parameters α, β and λ control the trade-off between the data fitting term and the penalties $\Phi(\mathbf{A})$, $\Psi(\mathbf{M})$ and $\Omega(\mathbf{B})$, described hereafter.

Abundance penalization: The abundance vectors $\mathbf{a}_n$ ($n = 1, \ldots, N$) are expected to vary smoothly between neighboring voxels, which motivates the use of a spatial smoothness penalization expressed in matrix form as

$$\Phi(\mathbf{A}) = \frac{1}{2}\|\mathbf{AS}\|_F^2 \tag{7}$$

where $\mathbf{S}$ is a matrix computing the first-order finite differences between the abundance vectors in a given voxel and the ones of its neighbors in each dimension.

Endmember penalization: Given an initial rough estimate $\mathbf{M}_0$ of the endmember matrix, the endmember penalization considered in this work promotes similarity between this initial guess and the recovered endmembers, through the following square distance

$$\Psi(\mathbf{M}) = \frac{1}{2}\|\mathbf{M} - \mathbf{M}_0\|_F^2. \tag{8}$$

ISBN 978-0-9928626-7-1 © EURASIP 2017

Variability penalization: For the study considered in this paper, the SBE variability is expected to be spatially localized and described by only a few contributions of the element basis in $\mathbf{V}$. Thus, a sparsity-promoting ℓ_1-norm penalization [10] is considered

$$\Omega(\mathbf{B}) = \|\mathbf{B}\|_1. \tag{9}$$

III. A PALM-BASED ALGORITHM

Since the problem (6) is genuinely nonconvex and nonsmooth but naturally exhibits a block-wise structure in terms of $\mathbf{A}$, $\mathbf{M}$ and $\mathbf{B}$, we propose to resort to the proximal alternating linearized minimization (PALM) algorithm [11]. It consists in performing proximal gradient descent steps with respect to each block, following the algorithmic sketch summarized in Algo. 1. Each step is detailed in what follows.

Algorithm 1: PSBE-LMM unmixing: PALM algorithm

Input: $\mathbf{Y}$
Initialization: $\mathbf{A}^0$, $\mathbf{M}^0$ and $\mathbf{B}^0$
begin
  $k \leftarrow 0$
  while *stopping criterion not satisfied* **do**
    $\mathbf{M}^{k+1} \leftarrow \mathcal{P}_+\left(\mathbf{M}^k - \frac{\gamma_M}{L_M^k}\nabla_{\mathbf{M}}\mathcal{J}(\mathbf{M}^k, \mathbf{A}^{k+1}, \mathbf{B}^k)\right)$
    $\mathbf{A}^{k+1} \leftarrow \mathcal{P}_{\mathcal{A}_R}\left(\mathbf{A}^k - \frac{\gamma_A}{L_A^k}\nabla_{\mathbf{A}}\mathcal{J}(\mathbf{M}^k, \mathbf{A}^k, \mathbf{B}^k)\right)$
    $\mathbf{B}^{k+1} \leftarrow$
      $\operatorname{prox}_{\frac{\lambda\gamma_B}{L_B^k}\|\cdot\|_1}\left(\mathbf{B}^k - \frac{\gamma_B}{L_B^k}\nabla_{\mathbf{B}}\mathcal{J}(\mathbf{M}^{k+1}, \mathbf{A}^{k+1}, \mathbf{B}^k)\right)$
    $k \leftarrow k+1$
Output: $\hat{\mathbf{A}} \triangleq \mathbf{A}^{k+1}$, $\hat{\mathbf{M}} \triangleq \mathbf{M}^{k+1}$ and $\hat{\mathbf{B}} \triangleq \mathbf{B}^{k+1}$.

A. Optimization with respect to $\boldsymbol{M}$

Given the assumptions in Section II, optimizing $\mathcal{J}$ with respect to $\mathbf{M}$ under the constraints (5) is expressed as

$$\mathbf{M}^{k+1} = \mathcal{P}_+\left(\mathbf{M}^k - \frac{\gamma_M}{L_M^k}\nabla_{\mathbf{M}}\mathcal{J}(\mathbf{M}^k, \mathbf{A}^{k+1}, \mathbf{B}^k)\right) \tag{10}$$

where $\mathcal{P}_+$ is the projection on the nonnegative plane $\{\mathbf{X}|\mathbf{X} \succeq \mathbf{0}_{L,R}\}$, $\gamma_M < 1$ is a constant assuring convergence and L_M^k is a bound on the Lipschitz constant of $\nabla_{\mathbf{M}}\mathcal{J}(\mathbf{M}^k, \mathbf{A}^{k+1}, \mathbf{B}^k)$ with

$$\begin{aligned}\nabla_{\mathbf{M}}\mathcal{J}(\mathbf{M}, \mathbf{A}, \mathbf{B}) = ((\mathbf{E}_1\mathbf{A} \circ \mathbf{VB})\mathbf{H} - \mathbf{Y})\,\tilde{\mathbf{A}}^T \\ +\mathbf{M}(\mathbf{AHH}^T\mathbf{A}^T) + \beta(\mathbf{M} - \mathbf{M}_0).\end{aligned} \tag{11}$$

The constant to be used is set as

$$L_M = \left\|\mathbf{AHH}^T\mathbf{A}^T\right\| + \beta. \tag{12}$$

B. Optimization with respect to $\boldsymbol{A}$

Similarly, under the constraints defined in (5), the updating rule for the abundance matrix is

$$\mathbf{A}^{k+1} = \mathcal{P}_{\mathcal{A}_R}\left(\mathbf{A}^k - \frac{\gamma_A}{L_A^k}\nabla_{\mathbf{A}}\mathcal{J}(\mathbf{M}^k, \mathbf{A}^k, \mathbf{B}^k)\right) \tag{13}$$

where $\mathcal{P}_{\mathcal{A}_R}$ is the projection onto $\mathcal{A}_R$, described by the abundance constraints in (5), which can be efficiently computed following the strategy in [12]. Moreover, $\gamma_A < 1$ is a constant that assures convergence of the algorithm and L_A^k is the Lipschitz constant of $\nabla_{\mathbf{A}}\mathcal{J}(\mathbf{M}^k, \mathbf{A}^k, \mathbf{B}^k)$ defined by

$$\nabla_{\mathbf{A}}\mathcal{J}(\mathbf{M}, \mathbf{A}, \mathbf{B}) = -\mathbf{M}^T(\mathbf{D}_A) - \mathbf{E}_1^T(\mathbf{D}_A \circ \mathbf{VB}) + \alpha\mathbf{ASS}^T,$$

with $\mathbf{D}_A = (\mathbf{Y} - \mathbf{MAH} - (\mathbf{E}_1\mathbf{A} \circ \mathbf{VB})\mathbf{H})\mathbf{H}^T$. The following value for the Lipschitz constant is defined

$$\begin{aligned}L_A = \alpha\left\|\mathbf{SS}^T\right\| + \|\mathbf{H}\|^2\Big(\left\|\mathbf{M}^T\mathbf{M}\right\| \\ + \|\mathbf{E}_1\|\,\|\mathbf{VB}\|\left(2\|\mathbf{M}\|_\infty + \|\mathbf{E}_1\|\,\|\mathbf{VB}\|_\infty\right)\Big)\end{aligned} \tag{14}$$

where the spectral norm $\|\mathbf{X}\| = \sigma_{\max}(\mathbf{X})$ is the largest singular value of $\mathbf{X}$ and $\|\mathbf{X}\|_\infty = \max_{1\le i\le m}\sum_{j=1}^n |x_{ij}|$ is the absolute value of the row-sum of the matrix entries. It is worthy to note that this value is not optimal, thus opening the way to possible accelerations of the updating rule.

C. Optimization with respect to $\mathbf{B}$

Finally, the updating rule of the variability matrix $\mathbf{B}$ can be written as

$$\mathbf{B}^{k+1} = \operatorname{prox}_{\frac{\lambda\gamma_B}{L_B^k}\|\cdot\|_1}\left(\mathbf{B}^k - \frac{\gamma_B}{L_B^k}\nabla_{\mathbf{B}}\mathcal{J}(\mathbf{M}^{k+1}, \mathbf{A}^{k+1}, \mathbf{B}^k)\right),$$

where the proximal operator $\operatorname{prox}_{\cdot\|\cdot\|_1}$ is the classical soft-thresholding operator, $\gamma_B < 1$ is a constant assuring convergence and L_B^k is the Lipschitz constant of $\nabla_{\mathbf{B}}\mathcal{J}(\mathbf{M}^{k+1}, \mathbf{A}^{k+1}, \mathbf{B}^k)$ defined as

$$\nabla_{\mathbf{B}}\mathcal{J}(\mathbf{M}, \mathbf{A}, \mathbf{B}) = V^T((\mathbf{E}_1\mathbf{A}) \circ (-\mathbf{Y} + \mathbf{MAH} + \Delta)\mathbf{H}^T)$$

with

$$L_B = \|\mathbf{E}_1\mathbf{A}\|_\infty^2\|\mathbf{V}\|^2\|\mathbf{H}\|^2.$$

IV. EXPERIMENTS

A. Data generation

The proposed method has been evaluated on a $128\times128\times64$-voxel synthetic dynamic PET image resulting from linear mixtures of $K = 4$ endmembers with $L = 20$ time-frames. The ground-truth of abundances and endmembers is generated from a numerical phantom with labeled ROIs of high resolution, for which real time activity curves measured on clinical acquisitions were used [13]. A PCA has been conducted on a learning set of physically-based simulated SBE signatures to describe its variability under the model (2). Thanks to a careful inspection of the eigenvalues associated with the corresponding eigenvectors, the basis $\mathbf{V}$ has been set to a unique element (i.e., $N_v = 1$). A non-zero SBE variability has been considered in the SBR branched into 4 subregions. In each of these subregions located in Fig. 1(left), the corresponding variability coefficients defining $\mathbf{B}$ have been randomly generated according to a Gaussian distribution with different mean values. A preliminary study conducted on the realistic replicas of [13] shows that the SNR ranges from approximately 10dB on the earlier frames to 20dB on the latter ones. As a consequence, an additive Gaussian noise with SNR$=$ 15dB has been considered in the following experiments.

ISBN 978-0-9928626-7-1 © EURASIP 2017

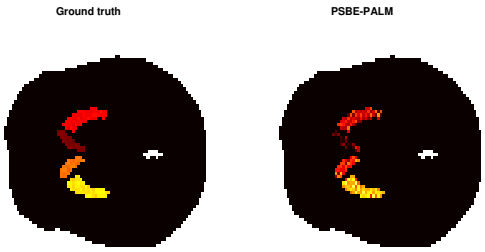

Fig. 1. Real (left) and estimated (right) SBE variability.

B. Compared methods

The proposed method, referred to as PSBE-PALM, has been compared to unmixing techniques borrowed from the hyperspectral imagery literature. First, the VCA algorithm [14] has been considered as an endmember extraction algorithm and coupled with the abundance estimation provided by SUnSAL [15]. Moreover, to illustrate the interest of considering SBE variability, a depreciated counterpart of the proposed PALM-based algorithm has been considered, without including the variability-related term in (3). This algorithm, referred to as LMM-PALM, only performs unmixing under a standard LMM. Both PALM-based algorithms have been initialized with K-means classification, where the SBE has been afterwards assigned the minimum TAC among the SBE TACs belonging to the learning set. The stopping criteria defined as the decreasing rate of the objective function has been set at ε is set to 10^{-3}. All algorithmic parameters are empirically tuned to the valued reported in Table IV-B. More automatized ways to choose these hyperparameters can be envisaged, such as cross-validation, grid search, random search and empirical Bayesian estimation but these choices seem to be sufficient to assess the performance of the methods.

TABLE I
ALGORITHMIC PARAMETERS.

	LMM-PALM	PSBE-PALM
α	0.010	0.010
β	0.010	0.010
λ	-	0.020
ε	0.001	0.001

Normalized mean square error (NMSE) have been considered to evaluate the estimation performance of the algorithms with respect to each quantity of interest

$$\text{NMSE}(\boldsymbol{\Theta}) = \frac{\|\hat{\boldsymbol{\Theta}} - \boldsymbol{\Theta}\|_F^2}{\|\boldsymbol{\Theta}\|_F^2} \tag{15}$$

where $\hat{\boldsymbol{\Theta}}$ is the estimated variable and $\boldsymbol{\Theta}$ the corresponding ground truth. In particular, to emphasize the role of the SBE variability, NMSEs have been computed separately for unknown parameters whose estimates are expected to be affected or non-affected by this variability. Thus, the estimation performance has been evaluated for *i*) the SBE abundance $\mathbf{A}_1 \triangleq [a_{1,1}, \ldots, a_{1,N}]$ and non-SBE abundance $\mathbf{A}_{2:K}$ (where $\mathbf{A}_{2:K}$ denotes the matrix $\mathbf{A}$ whose 1st row has been removed) and *ii*) the varying SBE signatures $\tilde{\mathbf{M}}_1 = [\tilde{\mathbf{m}}_{1,1}, \ldots, \tilde{\mathbf{m}}_{1,N}]$ with $\tilde{\mathbf{m}}_{1,n} \triangleq \bar{\mathbf{m}}_1 + \sum_{i=1}^{N_v} b_{i,n}\mathbf{v}_i$ and the non-SBE signatures $\mathbf{M}_{2:K}$ (where $\mathbf{M}_{2:K}$ denotes here the matrix $\mathbf{M}$ whose 1st column has been removed).

C. Results

The estimated abundance maps and associated TACs corresponding to the first two endmembers are shown in Fig. 2 for a given brain slice while Table II reports the NMSE. The three methods provides endmember estimates that are overall in good agreement with the expected kinetics of the specific-binding compartment (1st row) and grey matter (2nd row) as well as the white matter and blood (not depicted here for brevity). However, the proposed method outperforms both VCA/SUnSAL and LMM-PALM in all cases except for $\mathbf{A}_{2:K}$, in which LMM-PALM presents better performance. This result confirms the necessity of considering the variability. Moreover, the high correlation between endmember signatures makes LMM-PALM to converge to irrelevant local optima while PSBE-PALM provides better results in terms of the SBR abundance $\mathbf{a}_1$, by decreasing the variability error to almost 27%. However, some artifacts due to convolution process prevents the estimation error related to $\mathbf{B}$ to get smaller. Finally, while VCA associated with SUnSAL shows interesting results assessing the relevance of the unmixing concept for PET quantification, PALM-based results are even of higher interest. For all quantities of interest, both PALM-based algorithms outperform VCA/SUnSAL, where PSBE-PALM presents better results for the quantities related to the SBR and the remaining endmembers whereas LMM-PALM achieves smaller errors for the abundances outside the SBR. Therefore, this result shows the potential interest of considering a variability attached to the SBE in dynamic PET.

TABLE II
NMSE OF ESTIMATED PARAMETERS FOR VCA/SUNSAL, LMM-PALM AND PSBE-PALM.

	VCA/SUnSAL	LMM-PALM	PSBE-PALM
$\mathbf{a}_1$	0.518	0.469	**0.378**
$\mathbf{A}_{2:K}$	0.491	**0.454**	0.482
$\tilde{\mathbf{M}}^1$	0.507	0.264	**0.027**
$\mathbf{M}^{2:K}$	0.332	0.202	**0.174**
$\mathbf{B}$	-	-	0.273

V. CONCLUSION AND FUTURE WORKS

In this paper, a new linear mixing model including a perturbation on the SBE was introduced for the unmixing of dynamic PET images. Specific binding variations were modeled through a previously learnt basis and its respective matrix of proportions. Unmixing was performed by an alternating linearized minimization algorithm benefiting from proximal regularizations. The interest of the proposed solution was illustrated with simulations on synthetic yet physically-motivated data. In this study, PET noise was

ISBN 978-0-9928626-7-1 © EURASIP 2017

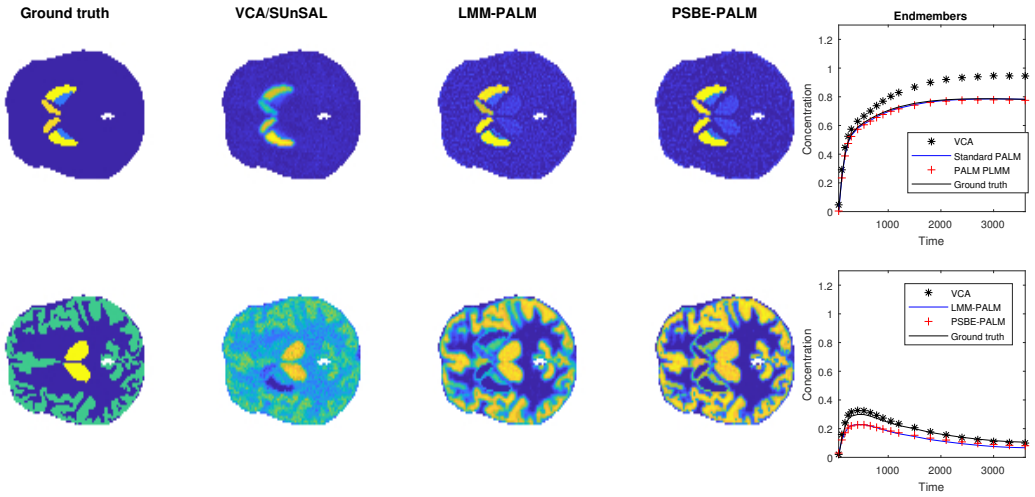

Fig. 2. Abundance maps (left) and corresponding TACs (right) associated with the SBR (top) and gray matter (bottom).

considered Gaussian. The inclusion of a Poisson-fitting divergence measure on the cost function will be considered in future work.

REFERENCES

[1] M. Naganawa, Y. Kimura, K. Ishii, K. Oda, K. Ishiwata, and A. Matani, "Extraction of a plasma time-activity curve from dynamic brain PET images based on independent component analysis," *IEEE Trans. Biomed. Eng.*, vol. 52, no. 2, pp. 201–210, 2005.

[2] C. Schiepers, W. Chen, M. Dahlbom, T. Cloughesy, C. K. Hoh, and S.-C. Huang, "18F-fluorothymidine kinetics of malignant brain tumors," *Eur. J. Nuclear Med. Molecular Imag.*, vol. 34, no. 7, pp. 1003–1011, Feb 2007.

[3] M. E. Kamasak, "Computation of variance in compartment model parameter estimates from dynamic PET data," *Proc. IEEE Int. Symp. Biomed. Imag. (ISBI)*, 2012.

[4] R. Boellaard, A. van Lingen, and A. A. Lammertsma, "Experimental and clinical evaluation of iterative reconstruction (OSEM) in dynamic PET: Quantitative characteristics and effects on kinetic modeling," *J. Nuclear Med.*, vol. 42, no. 5, pp. 808–817, 2001.

[5] J. M. Bioucas-Dias, A. Plaza, N. Dobigeon, M. Parente, Q. Du, P. Gader, and J. Chanussot, "Hyperspectral unmixing overview: Geometrical, statistical, and sparse regression-based approaches," *IEEE J. Sel. Topics Appl. Earth Observations Remote Sens.*, vol. 5, no. 2, pp. 354–379, April 2012.

[6] N. Dobigeon and N. Brun, "Spectral mixture analysis of EELS spectrum-images," *Ultramicroscopy*, vol. 120, pp. 25–34, Sept. 2012.

[7] J. S. Lee, D. D. Lee, S. Choi, K. S. Park, and D. S. Lee, "Non-negative matrix factorization of dynamic images in nuclear medicine," in *IEEE Nuclear Science Symposium Conference Record*. IEEE, 2001.

[8] P.-A. Thouvenin, N. Dobigeon, and J.-Y. Tourneret, "Hyperspectral unmixing with spectral variability using a perturbed linear mixing model," *IEEE Trans. Signal Process.*, vol. 64, no. 2, pp. 525–538, 2016.

[9] S.-U. Park, N. Dobigeon, and A. O. Hero, "Variational semi-blind sparse deconvolution with orthogonal kernel bases and its application to MRFM," *Signal Process.*, vol. 94, pp. 386–400, Jan. 2014.

[10] R. Tibshrani, "Regression shrinkage and selection via the lasso," *Journal of the Royal Statistical Society*, vol. 58, no. 1, pp. 267–288, 1996.

[11] J. Bolte, S. Sabach, and M. Teboulle, "Proximal alternating linearized minimization for nonconvex and nonsmooth problems," *Mathematical Programming*, vol. 146, no. 1-2, pp. 459–494, Jul 2013.

[12] L. Condat, "Fast projection onto the simplex and the l_1-ball," *Math. Program.*, vol. 158, no. 1-2, pp. 575–585, Sep 2015.

[13] S. Stute, C. Tauber, C. Leroy, M. Bottlaender, V. Brulon, and C. Comtat, "Analytical simulations of dynamic PET scans with realistic count rates properties," *IEEE Nuclear Sci. Symp. Medical Imag. Conf.*, pp. 113–122, May 2015.

[14] J. Nascimento and J. Dias, "Vertex component analysis: a fast algorithm to unmix hyperspectral data," *IEEE Trans. Geosci. Remote Sens.*, vol. 43, no. 4, pp. 898–910, Apr 2005.

[15] J. M. Bioucas-Dias and M. A. T. Figueiredo, "Alternating direction algorithms for constrained sparse regression: Application to hyperspectral unmixing," in *Proc. IEEE GRSS Workshop Hyperspectral Image SIgnal Process.: Evolution in Remote Sens. (WHISPERS)*, 2010.

ISBN 978-0-9928626-7-1 © EURASIP 2017